

Time-resolved 3D Capture of Non-stationary Gas Flows

Bradley Atcheson¹, Ivo Ihrke¹, Wolfgang Heidrich¹, Art Tevs², Derek Bradley¹, Marcus Magnor³, Hans-Peter Seidel²

1) The University of British Columbia, 2) Max-Planck-Institut für Informatik, 3) Braunschweig University

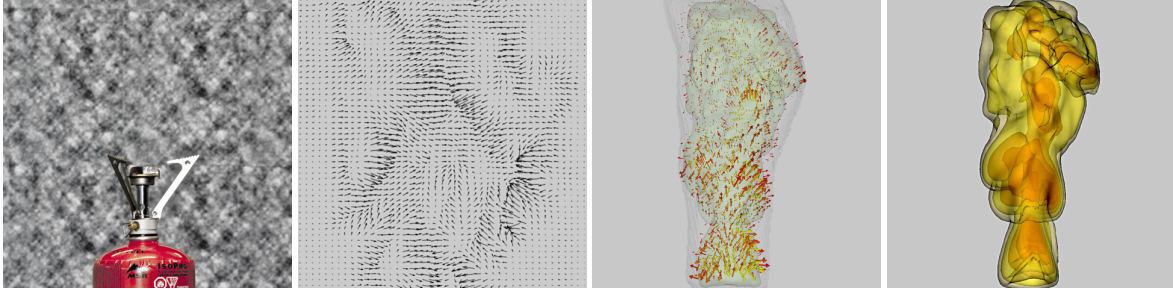


Figure 1: Measurements of the hot air flow above a gas burner. Far left: a camera observes distortions of a high frequency background caused by a hot air plume. Center left: a quiver plot of the 2D distortions extracted using optical flow algorithms. Center right: a visualization of the 3D gradient field tomographically reconstructed from 16 cameras. Far right: volume rendering of the final refractive index field after Poisson integration.

Abstract

Fluid simulation is one of the most active research areas in computer graphics. However, it remains difficult to obtain measurements of real fluid flows for validation of the simulated data.

In this paper, we take a step in the direction of capturing flow data for such purposes. Specifically, we present the first time-resolved Schlieren tomography system for capturing full 3D, non-stationary gas flows on a dense volumetric grid. Schlieren tomography uses 2D ray deflection measurements to reconstruct a time-varying grid of 3D refractive index values, which directly correspond to physical properties of the flow. We derive a new solution for this reconstruction problem that lends itself to efficient algorithms that robustly work with relatively small numbers of cameras. Our physical system is easy to set up, and consists of an array of relatively low cost rolling-shutter camcorders that are synchronized with a new approach. We demonstrate our method with real measurements, and analyze precision with synthetic data for which ground truth information is available.

CR Categories: I.3.3 [COMPUTER GRAPHICS]: Picture/Image Generation—Digitizing and scanning; I.4.1 [IMAGE PROCESSING AND COMPUTER VISION]: Digitization and Image Capture—Imaging geometry.

Keywords: Image Processing, Computational Cameras and Optics, Object Scanning/Acquisition

1 Introduction

Computer graphics researchers have for a long time been interested in capturing properties and behaviors of real-world objects, both for

direct use of the captured data in rendering, and, maybe even more importantly, for deepening the understanding of the principles underlying specific phenomena. A significant body of work has been developed for measuring aspects such as BRDFs (e.g. [Ward 1992; Marschner et al. 1999; Matusik et al. 2003], and many more), subsurface and volumetric scattering (e.g. [Jensen et al. 2001; Goesele et al. 2004; Hawkins et al. 2005; Narasimhan et al. 2006]), human performance (e.g. [de Aguiar et al. 2008; Vlasic et al. 2008]), and cloth (e.g. [White et al. 2007; Scholz et al. 2005]).

However, computer graphics research has so far paid surprisingly little attention to the capture of fluids. The fluid imaging community has, of course, considered this problem. However, their measurements are typically either sparse, or only capture 2D slices or projections of the flow. Recent work on Schlieren tomography (see Section 2) has considered dense volumetric reconstructions, but only for stationary flows (e.g. [Goldhahn and Seume 2007]).

In this paper, we present the first *volumetric, time-resolved* Schlieren imaging system. For the first time, our approach allows for capturing time-varying density differences of a non-stationary gas flow on a dense grid. From this data, one can infer further information such as temperature and pressure distributions. We believe that such ground truth data for non-trivial scenes will be interesting for the very active fluid simulation community. Our technical contributions include:

- the first time-resolved system for Schlieren tomography on non-stationary flows,
- a Background-Oriented Schlieren imaging system using inexpensive rolling shutter consumer cameras, including a novel synchronization method for such a setup,
- a novel visual-hull constrained algorithm for the Schlieren tomography problem, including mask estimation from 2D ray deflection data, visual hull constrained tomographic reconstruction, and visual hull constrained anisotropic Poisson integration, and
- the application of this new reconstruction algorithm to the reconstruction of high quality 3D density information from a modest number of views.

2 Related Work

Scanning of transparent objects has recently been the focus of a number of research efforts in computer graphics and machine vision [Ben-Ezra and Nayar 2003; Miyazaki and Ikeuchi 2005; Morris and Kutulakos 2005; Kutulakos and Steger 2005; Trifonov et al. 2006]. This work is related to our approach, in so far as we focus on transparent gas flows. However, the existing literature in this area either eliminates or ignores refraction, or assumes that refraction happens only at discrete interfaces between different materials. In gaseous flows, however, the refractive index of the gas varies smoothly across the volume, causing rays to bend continuously.

As a result, most work on scanning transparent objects deals exclusively with solids. Only recently, certain classes of dynamic transparent objects have been considered, including liquids [Ihrke et al. 2005] and flames [Hasinoff and Kutulakos 2007; Ihrke and Magnor 2004]. In the former case, the refractive index of the object is required to be constant, while in the latter refraction is ignored altogether. Ihrke and Magnor’s work is also the first to show visual hull constrained tomography, although their method needs to be significantly extended to work with Schlieren data.

Dynamic participating media, such as smoke, have been the subject of capturing efforts in computer graphics [Hawkins et al. 2005; Fuchs et al. 2006]. Such work could potentially be extended for capturing the underlying fluid structure. However, it would be necessary to employ some form of tracking on the scattering properties over time, since the scattering properties are a characteristic of particles carried with the fluid, as opposed to a characteristic of the fluid itself. Such tracking has not been attempted in the graphics literature, although it would be conceptually similar to particle imaging velocimetry, discussed next. An additional challenge with this approach would be the temporal shearing introduced by time-sequential imaging of planes [Hawkins et al. 2005], or the sparseness of the measured data [Fuchs et al. 2006].

Particle Imaging Velocimetry (PIV) is a method developed in the fluid imaging community. Macroscopic particles are injected into the flow, and illuminated by a sheet of laser light. The 2D motion of illuminated particles in the laser plane is then tracked with optical flow algorithms. A good overview of the PIV method can be found in the survey by Grant [1997].

The PIV approach can be extended to volumetric imaging by sweeping the laser plane through the volume (see, e.g. [Van Vliet et al. 2004]), although it remains very challenging to accurately capture out-of-plane motion. Similar to the work by Hawkins et al. [2005], the 3D variant also suffers from temporal shearing, which may be compensated for by a three-dimensional optical flow estimate and subsequent warping. Finally, injecting particles to maintain a uniform distribution within the flow is an extremely challenging problem in practice.

Schlieren imaging and tomography is a passive imaging technique for dynamically changing refractive index fields that has been developed in the fluid imaging community over several decades.¹ The original setups from the 1940s require high-quality optical mirrors and lenses of a size comparable to the volume under investigation [Schardin 1942]. Although these kinds of systems are still in use even today [Settles 2001], they are expensive and difficult to configure. It is also difficult to perform *quantitative* rather than qualitative measurements with them, although it is possible with careful calibration [Howes 1984].

¹The German word “Schlieren” means “streaks” and refers to the optical distortions caused by inhomogeneous refractive index fields.

These shortcomings have prompted the development of the much simpler Background Oriented Schlieren (BOS) technique in recent years [Dalziel et al. 2000; Richard and Raffel 2001; Meier 2002; Elsinga et al. 2004]. In the BOS setup, a digital camera observes a high-frequency background through the volume under investigation. Optical flow algorithms are used to compute a per-pixel deflection vector with respect to an undistorted reference background. Since only a single image is required for each geometry, the method is suitable for imaging dynamic flows.

If 2D deflection data for *multiple* viewpoints is available from either BOS, one of the original Schlieren setups, or other sources, then it is possible to use tomographic reconstruction to obtain a volumetric estimate of the refractive index field [Venkatakrishnan and Meier 2004; Schwarz 1996]. In practice, however, it is challenging to come up with an experimental setup that can provide enough views for standard tomographic reconstruction algorithms. Therefore, the only actual implementations of this principle have so far been limited to certain classes of flows that reduce the requirements on the number of cameras involved. For example, rotationally symmetric flows can be tomographically reconstructed from a single view [Faris and Byer 1988; Venkatakrishnan and Meier 2004], while stationary flows can be acquired with a single camera that moves around the scan volume [Schwarz 1996; Agrawal et al. 1999; Goldhahn and Seume 2007].

One of the key contributions of our work is to develop a visual-hull constrained tomographic reconstruction pipeline for Schlieren imaging that produces high quality reconstructions from as little as 16 views. As a result, we can for the first time build an acquisition system that allows us to capture full time-resolved, non-stationary flows from BOS measurements.

3 Overview

Our method for capturing gas flow builds and improves upon the Background Oriented Schlieren (BOS) method outlined above. In the following we provide a brief overview of the image formation process for BOS, as well as the 2D imaging and 3D reconstruction stages, before delving into the details of our method in the following sections.

Image formation in optically inhomogeneous media is governed by continuous refraction. The propagation of light in inhomogeneous media is described by the *ray equation of geometric optics*:

$$\frac{d}{ds} \left(n \frac{d\mathbf{x}}{ds} \right) = \nabla n. \quad (1)$$

Here, n describes an inhomogeneous refractive index field, \mathbf{x} is the position of a ‘particle’ traversing the light ray, and ds is the differential path length along the ray. Equation 1 has been employed in computer graphics to render atmospheric effects [Stam and Langenou 1996; Gutierrez et al. 2006] or complex refractive objects [Ihrke et al. 2007]. The ray equation can be re-formulated as a system of coupled first-order ODEs [Ihrke et al. 2007]:

$$n \frac{d\mathbf{x}}{ds} = \mathbf{d}, \quad \frac{d\mathbf{d}}{ds} = \nabla n, \quad (2)$$

where the vector \mathbf{d} describes the local ray direction scaled by the local refractive index. In gas flows, where $n \approx 1$, it is common to approximate \mathbf{d} by a unit vector [Goldhahn and Seume 2007].

Equation 2 can be integrated to obtain an equation that relates the gradient of the refractive index field to three-dimensional ray deflections:

$$\mathbf{d}^{out} = \int_c \nabla n \, ds + \mathbf{d}^{in}. \quad (3)$$

Here, c describes the ray path and vectors \mathbf{d}^{in} and \mathbf{d}^{out} denote the incoming and outgoing ray directions with respect to the optically inhomogeneous region (see Figure 2). Equation 3 forms the basis of both 2D BOS measurements and the 3D reconstruction.

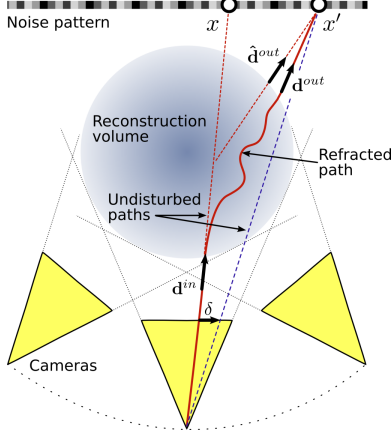


Figure 2: Principle of the deflection sensor: A plane with a high-frequency dot pattern is placed behind the scene of interest and an image is recorded without the object (dashed red line). Then the inhomogeneous refractive index field is inserted between the camera and the background plane. Another image is taken and the deflection of the light rays in the image plane is computed using optical flow.

2D deflection sensing (Section 4) involves a BOS imaging setup, using digital video cameras to observe a high-frequency background through the flow under investigation. Per-pixel deflections are caused by refraction due to spatial variations in the volume densities inside the flow (Equation 3, Figure 2). These deflections are captured with an optical flow algorithm. The resulting (2D) deflection vectors δ can be directly used to visualize 2D projections of the flow.

Figure 2 shows an (exaggerated) diagram of such a setup. In this case, the volume, indicated by the shaded region, consists of air that has a lower density than its surroundings (e.g. a plume of hot air). As a result, camera rays are bent away from the center of the volume, intersecting a background plane in point x' rather than x for an undistorted ray. The corresponding 2D displacement δ is measured by the BOS approach.

3D tomographic reconstruction (Section 5) is based on a set of deflection images taken from different viewpoints. Equation 3 shows that the individual deflection vectors measured by 2D BOS imaging represent line integrals over the gradient of the refractive indices within the volume under investigation. As such, the refractive index gradients can, in principle, be recovered through tomographic reconstruction methods similar to those used in medical imaging [Kak and Slaney 2001]. However, the limited number of cameras in a practical BOS setup results in a significantly sparser sampling of the ray space than in the medical setting. We account for this sparseness by developing a new reconstruction algorithm that is robust under such circumstances. Another advantage of our reconstruction algorithm is that, unlike methods such as the Radon transform [Kak and Slaney 2001], it can work with general camera positions and orientations.

Once the refractive index gradients have been reconstructed, they can be integrated into a volumetric representation of refractive indices using a Poisson solver. Finally, these refractive indices directly correspond to volume densities, which are an inherent property of the flow itself. From these volume density measurements, additional information such as pressure and temperature distributions can be extracted under certain assumptions.

4 Background Oriented Schlieren Imaging

In this section we describe the measurement setup, its calibration and synchronization, and the estimation of the BOS deflection vectors.

Capture setup. Our measurement setup, depicted in Figure 3, consists of 16 high definition (1440×1080 , interlaced) Sony HDR-SR7 camcorders. The cameras surround a measurement volume of roughly $30 \times 15 \times 15$ cm in a 180° arc. Behind the scan volume we place high frequency noise patterns that are illuminated with both sunlight and 800 W halogen stage lights. Strong lighting is required to keep exposure times as short as possible so as to minimize motion blur. Overhead fluorescent lights would flicker out of sync with the cameras, with the resulting spatially-varying illumination changes in the images producing optical flow artifacts.

In order to maximize the detectable light ray deflection, the background should be positioned as far as possible behind the measurement volume. The cameras should use a long focal length, and must be focused on the background plane for the optical flow to work reliably. This means that the flow volume itself will be out of focus unless the camera aperture can be held small, or the cameras are moved back from the volume as well. Since we require a large aperture for reasons of light sensitivity, we compromised by positioning the measurement volume in the center of a 5 m diameter ring formed by the cameras and backgrounds, as shown in Figure 3. The extrinsic and intrinsic parameters of all cameras are calibrated with standard techniques [Zhang 1999].

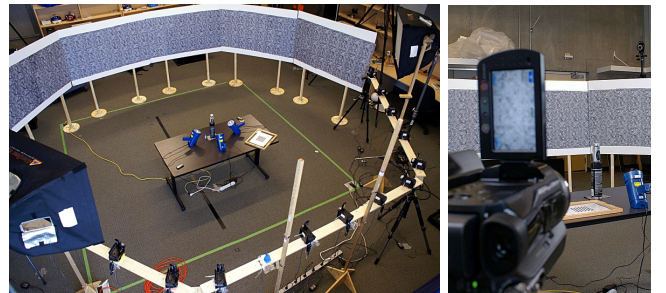


Figure 3: Photographs of our acquisition setup.

In previous work [Atcheson et al. 2008], we showed that Wavelet Noise [Cook and DeRose 2005] makes for an ideal high-frequency background for BOS imaging, since it contains information on a wide range of spectral bands. As such, a camera recording a Wavelet Noise pattern will observe dense, locally distinct features everywhere in the image, independent of the magnification factor. This decoupling of camera and pattern resolution drastically reduces the effort for setting up a BOS system.

Alternatively, dynamic environment matting techniques [Chuang et al. 2000] could be employed to measure the deflection vectors. Note, however, that the accuracy would be very limited due to quantization and compression noise introduced by the cameras.

Computing BOS deflections. In most existing BOS systems deflection vectors from a distorted background to a “clean” reference image are computed using a simple cross-correlation window matching [Kindler et al. 2007]. We recently demonstrated that gradient-based optical flow methods such as Lucas-Kanade [1981] or Horn-Schunck [1981] produce significantly better results, especially when combined with Wavelet Noise background patterns [Atcheson et al. 2008]. In that work, we also found that variational optical flow approaches such as Brox et al. [2004], do *not* perform as well as the simpler gradient based methods due to over-smoothing. We believe this behavior is due to the different statistics of BOS datasets, which are continuous but may have high frequency areas, as compared to typical optical flow scenes, which are often smooth with isolated discontinuities.

In our experiments for the present work, we chose Lucas-Kanade optical flow to determine the BOS deflection vectors. Although our earlier experiments show that Horn-Schunck produces slightly better results with ideal parameters settings, we found Lucas-Kanade less sensitive to parameter selection, which is a highly desirable property when processing thousands of frames recorded by multiple cameras. For each camera we obtain a 2D displacement vector field, as illustrated in Figure 4. The input video frames are compared to a reference background to produce a 2D optical flow field, which is then smoothed and filtered to remove outliers.

After computing optical flow, we downsample the resulting 2D deflection fields to 480×270 . This reduced resolution is sufficient for the tomographic reconstruction that follows, and the downsampling eases the memory requirements that result from the use of an array of 16 cameras. However, we found it important to perform the downsampling *after* the optical flow estimation, instead of estimating the optical flow on downsampled original images. The latter approach resulted in significantly poorer optical flow estimates in our experiments.

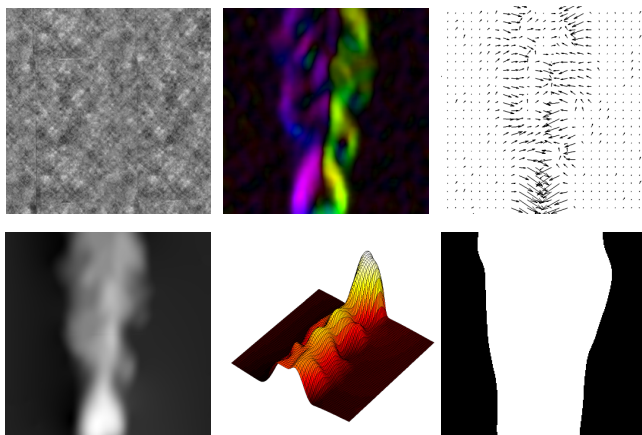


Figure 4: Top row: input camera image (left); visualizations of the recovered 2D deflection vectors as color coding (center) and a quiver plot (right). Bottom row: Poisson integrated deflection vectors (left) are thresholded (center), and after smoothing and dilation produce a binary mask (right) for generating a conservative visual hull of the plume.

Visual hull generation. The tomographic reconstruction algorithm described in Section 5 requires as input the visual hull of the 3D flow based on the observed 2D optical flow. To generate this visual hull, we need to create a conservative binary mask of the flow for each camera and each frame in the sequence. Note that we cannot simply segment the gas flow from the static background by thresholding the length of the 2D optical flow vectors, since the 2D

deflections can be zero even if the 3D gradient is not. Equation 3 shows that this happens when the camera ray is parallel to the gradient of the refractive index. Figure 4 indicates that this happens in practice for rays passing near the center of the plume.

Note, however, that the optical flows observed by a BOS system follow a specific pattern, where the direction of the optical flow depends on the relative position with respect to a plume of higher or lower density. Consider the case of a hot air plume above a candle or similar source. Since hot air has lower density and thus lower refractive index, light will tend to be refracted away from the center of the plume, i.e. primarily to the left on the left side of the plume, and to the right on the right side of the plume (see color coding in Figure 4). Therefore, we can segment the plume from the background by first Poisson integrating the optical flow field, and then thresholding the resulting scalar field. The threshold value is chosen automatically to include a given percentage of pixels across the entire sequence, which ensures approximate consistency across all cameras. Finally, a spatio-temporal dilation is applied to the masks to remove any remaining temporal artifacts and make the mask a conservative estimate compared to the true visual hull. The bottom row of Figure 4 shows the integrated deflection vectors, the thresholding, as well as the final mask after cleanup.

Camera synchronization. A fundamental obstacle to using inexpensive consumer camcorders for camera arrays is that such cameras do not support synchronization with a common trigger signal. Moreover, our cameras, like many consumer devices, use a rolling shutter, in which the exposure periods for the individual scanlines start at different times, such that each scanline has completed exposure just in time for reading out the scanline. As observed by Wilburn et al. [2004], this process results in a shearing that needs to be compensated for.

It turns out that the rolling shutter problem and the camera synchronization can be solved in a single resampling step. Since the rolling shutter causes a shear in the spatio-temporal volume, we can compensate for it by extracting slices of constant time from this sheared volume. In order to compensate for frame-to-frame motion, we compute a linear warp function between successive captured frames using optical flow. We then extract a synthetic time slice from the spatio-temporal volume by applying this warp with a different weight for each scanline. The weights correspond to the different time offsets at which the scanlines in the original images have been exposed. Moreover, if the subframe time offset between multiple cameras is known, the synthetic times for the extracted slices can be chosen such that the resulting images from all cameras correspond to the same virtual point in time (see Figure 5).

In order to find the subframe time offset between all 16 cameras, we can use a single synchronization event that is visible in all cameras. In our case, we use a stroboscope that emits a single flash of light. In each camera, this flash shows up as a sharply delineated block of bright scanlines (see Figure 5). The boundaries of this block of scanlines provide the required synchronization information.

Unlike Wilburn et al. [2004], our approach does not require scanlines from multiple cameras to create instantaneous frames. Instead, we are able to operate on individual cameras, while at the same time dealing with inter-camera synchronization. As mentioned above, we can extract synthetic exposure images after linear warping (Figure 5). Unfortunately, warping the raw video directly is undesirable, since resampling would destroy the high frequency information required to reliably estimate the optical flow. However, the optical flow fields are much smoother than the background noise patterns, so we warp between these instead.

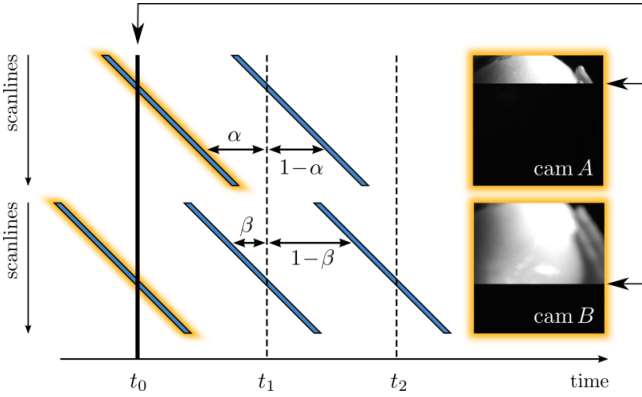


Figure 5: Rolling shutter cameras use individually chosen exposure intervals for each scanline, resulting in a spatio-temporal shear of the frames in the video sequence for each camera. This shear can be compensated for by temporal warping, where the weights for each camera and scanline are derived from a common synchronization event in one of the frames from each camera. In our case, the synchronization event is a stroboscope flash that illuminates a sharply delineated block of scanlines in this reference frame.

5 Tomographic Reconstruction

According to Equation 3, the deflection vectors acquired with the BOS technique from the last section contain information about the three-dimensional refractive index gradient within a gas flow. If BOS deflection vectors are available from multiple view points simultaneously, it is possible to set up a tomographic reconstruction problem to recover the three-dimensional gradient information. Integrating the recovered gradients results in a three-dimensional refractive index distribution.

In the following, we derive the necessary equations, discuss discretization issues and the choice of numerical techniques for their solution.

Gradient Field Tomography is based on Equation 3, relating three-dimensional ray deflections to three-dimensional refractive index gradients via line integrals. With the BOS setup it is possible to measure two-dimensional projections of the three-dimensional ray deflections.

We discretize the unknown vector-valued function ∇n using a set of normalized basis functions ϕ_i with unknown coefficient vectors \mathbf{n}_i ,

$$\widehat{\nabla n} = \begin{pmatrix} \sum_i n_i^x \phi_i \\ \sum_i n_i^y \phi_i \\ \sum_i n_i^z \phi_i \end{pmatrix} = \sum_i \mathbf{n}_i \phi_i,$$

thus rewriting Equation 3 as follows:

$$\int_c \widehat{\nabla n} ds = \int_c \sum_i \mathbf{n}_i \phi_i ds = \sum_i \mathbf{n}_i \int_c \phi_i ds = \mathbf{d}^{out} - \mathbf{d}^{in}. \quad (4)$$

Here $\mathbf{n}_i = (n_i^x, n_i^y, n_i^z)$ is a three component coefficient vector, independently parameterizing the three gradient components. The discretization results in a separate system of linear equations for each of the gradient components:

$$\mathbf{S} \mathbf{n}_{(x,y,z)} = \mathbf{d}^{out}_{(x,y,z)} - \mathbf{d}^{in}_{(x,y,z)}. \quad (5)$$

Note that matrix \mathbf{S} is the same for each of the gradient components: we have to solve for different right hand sides only. The entries of

matrix \mathbf{S} consist of line integrals over the basis functions:

$$\mathbf{S} = \begin{pmatrix} \int_{c_1} \phi_1 ds & \dots & \int_{c_1} \phi_{n_b} ds \\ \int_{c_2} \phi_1 ds & \dots & \int_{c_2} \phi_{n_b} ds \\ \vdots & \vdots & \vdots \\ \int_{c_{n_p}} \phi_1 ds & \dots & \int_{c_{n_p}} \phi_{n_b} ds \end{pmatrix}, \quad (6)$$

where n_b is the number of basis functions, and n_p is the number of deflection measurements from all camera views simultaneously. We approximate the integrals in the entries of the linear system by ray-casting and sampling the basis functions. The curved rays $c_1 \dots c_{n_p}$ are approximated by straight rays. This *paraxial* approximation is consistent with standard practices in Schlieren tomography (e.g. [Goldhahn and Seume 2007]), and is justified by the very small ray deflections in gas flows. Simulations of our setup showed a mean deviation from a straight path of less than 1/10 of a voxel in a 128^3 discretization of typical flow data (i.e. less than about 0.1 mm).

The small ray deflections also allow us to make another approximation. We compute an estimate $\hat{\mathbf{d}}^{out}$ of the deflection vector \mathbf{d}^{out} as the vector from a point on the original (undeflected) camera ray to the point on the background seen by the deflected ray (see Figure 2). This assumes a single discrete refraction event near the center of the reconstruction volume, as opposed to a continuous bending of the ray throughout the volume. This approximation is justified by both the small magnitude of the deflections inside the scan volume, as well as the small diameter of that volume compared to its distance from the background. In Section 6 we show that the reconstruction results obtained using this approximation are in good agreement with those produced with the true deflection vector.

The choice of basis functions is important for the tractability of the problem. We employ radially symmetric linear basis functions $\hat{\phi}_i = \max(0, 1 - r)$ with one voxel overlap in each dimension. Here, r is the radius from the center of the basis function. The normalized functions are of the form $\phi_i = \hat{\phi}_i / \sum_j \hat{\phi}_j$. Using these functions preserves the sparseness of the linear system while still allowing for data interpolation in the three-dimensional solution space. We arrange the basis functions on a regular grid, excluding basis functions with a support completely outside of the visual hull [Laurentini 1994]. Visual hull restricted tomography was introduced in the context of flame reconstruction [Ihrke and Magnor 2004] and is useful in obtaining high quality tomographic reconstructions from a sparse set of input views. The visual hull serves as an effective regularization on the shape of the reconstructed volume and suppresses projection artifacts.

Integration of the Gradient Field is analogous to computing a surface from (potentially noisy) normals. We use a discretized version of the definition of the Laplacian operator

$$\Delta n = \nabla \cdot \widehat{\nabla n} \quad (7)$$

to compute n . The left hand side of Equation 7 is discretized, while the right hand side is computed using the recovered $\widehat{\nabla n}$. The resulting Poisson equation is solved for n .

The basic Poisson integration scheme assumes a consistent set of gradient vectors, i.e. $\nabla \times \nabla n = 0$. However, due to measurement errors, the reconstructed vector field does not, in general, meet this condition. As a result, the standard Poisson formulation often results in overshoots by attempting to fit inconsistent gradient vectors in a least-squares sense. Agrawal et al. [2006] present a technique for integrating inconsistent gradient fields in two dimensions. Their method is based on anisotropic diffusion and can be formulated as

$$\nabla \cdot (\mathbf{D} \nabla n) = \nabla \cdot (\widehat{\nabla n}). \quad (8)$$

Here \mathbf{D} is a diffusion tensor that weighs gradient information from different directions. For standard Poisson integration $\mathbf{D} = \mathbf{I}$. In our work we use an edge-preserving, anisotropic diffusion tensor similar to [Weickert 1996; Agrawal et al. 2006], extending it to three dimensions. This involves the more complex analysis of face, edge and corner situations in three dimensions compared to the 2D case where only corners and straight edges have to be dealt with. Intuitively, \mathbf{D} prefers gradient information taken from similar isosurfaces of the integrated function and weighs down gradient information orthogonal to it. The exact definition of \mathbf{D} and its computation can be found in the Appendix.

We discretize Equation 8 using a combination of first-order forward and backward differences, which results in a numerical approximation similar to central-differences. The anisotropic Poisson equation is again discretized within the visual hull only. This measure saves computation time and avoids blurring of the result into the surrounding empty volume. We use Dirichlet boundary conditions outside the visual hull with $n = n_{air} = 1.00029$.

The resulting linear system is large, sparse, and positive definite. It can be solved most efficiently with multi-grid solvers. However, since we have to perform the integration only once per frame we use a less efficient but easier to implement Jacobi-preconditioned Conjugate Gradient method [Barrett et al. 1994].

6 Results

We evaluated our Schlieren imaging and tomographic reconstruction system both quantitatively with synthetic data, and qualitatively through measurements.

Synthetic data allows us to judge the precision of the proposed approach by comparisons with ground truth information. To this end, we process known density fields to analyze the robustness of the individual stages (2D optical flow, 3D tomography, and Poisson solver), as well as the sensitivity to parameters such as the number of cameras. We ran our analysis on both fluid data that was generated with a fluid simulator, as well as data captured in our setup, which was subsequently used as ground truth in a simulation. The specific numbers presented here are from a particular, but representative, fuel injection data set [DFG, SFB 382], shown in Figure 6. For all simulation results, we report errors both as relative RMS errors, as well as peak signal-to-noise ratio ($\text{PSNR} = 20 \cdot \log_{10} \frac{1}{\text{RMS}}$).

First, we evaluated the impact of the Poisson solver, and its interaction with the discretization of the normal field. In many gradient-based algorithms, the Poisson solver operates on a gradient field that has been numerically computed. In such a setting, it is possible to carefully select the discretization of the Poisson solver to match that of the normal estimation, such that the result is exact up to floating point precision. However, for the measured gradient fields in our setting, the discretization of the normal field is implicit in the measurement setup and tomographic reconstruction, and thus the discretization in the Poisson solver will introduce a larger numerical error. To estimate this error, we started from the ground truth volume data, computed the gradient field with an “unknown” discretization, and used the anisotropic Poisson solver to compute an estimate of the original volume. We obtain a PSNR of 42.15 dB (RMS error of 0.78%) on the fuel injection data set, and similar numbers on other data. These numbers provide a baseline for the quality that can be achieved with perfect optical flow estimation, an unlimited number of views, and perfect tomographic reconstruction. A comparison between the ground truth data and the Poisson reconstruction is shown in Figure 6.

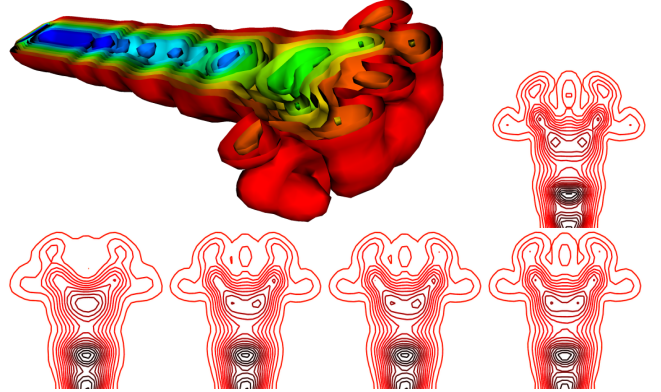


Figure 6: Top row: 3D rendering of the ground-truth synthetic fuel injection dataset, and an iso-line rendering from a cross-section around the turbulent part. Bottom row: the same cross-section for various simulation results. The first three images from left to right represent tomographic reconstructions from optical flow data with 8, 16, and 32 cameras. The rightmost image shows a Poisson integration from ground truth 3D gradients.

Simulation errors for tomographic reconstruction						
Direction estimate	Half ring setup					
	8 Cameras		16 Cameras		32 Cameras	
Ground truth (\mathbf{d}^{out})	40.55	0.94%	41.29	0.86%	41.39	0.85%
Approximate ($\hat{\mathbf{d}}^{out}$)	40.43	0.97%	40.73	0.91%	40.76	0.91%
Optical flow	39.29	1.09%	39.84	1.02%	39.88	1.01%
Full ring setup						
Direction estimate	7 Cameras		15 Cameras		31 Cameras	
	PSNR	RMS	PSNR	RMS	PSNR	RMS
Approximate ($\hat{\mathbf{d}}^{out}$)	40.03	1.00%	40.74	0.92%	40.83	0.91%

Table 1: Errors statistics for experiments with synthetic data. See text for a detailed discussion.

Next, we analyzed the impact of the number of cameras on the tomographic reconstruction part. We ray-traced light paths from virtual cameras through the ground truth volume, and recorded the direction of the ray as it exits the volume. These direction values \mathbf{d}^{out} were then used for the tomographic reconstruction algorithm, and integrated using the anisotropic Poisson solver. The resulting errors are shown in the first row of Table 1. The total reconstruction error for 16 cameras (PSNR: 41.29 dB, RMS: 0.86%) is already very close to the error bound obtained from the Poisson integration alone. Additional cameras do not result in significant further reductions of error. While the numbers depend somewhat on the volume resolution and the complexity of the flow, we found that 16 cameras generally provide the best tradeoff between hardware requirements and precision.

In the previous simulation we assumed that the exact refracted light direction \mathbf{d}^{out} was known. However, the deflection measurements obtained by BOS correspond to an approximation $\hat{\mathbf{d}}^{out}$ of this direction (see Figure 2), that only matches the true direction if the ray refracts in a single point rather than being continuously deflected over a finite volume. However, since the scan volume is small compared to its distance from the background, and since the ray deflections are small as well, one expects $\hat{\mathbf{d}}^{out}$ to be a good enough approximation. This hypothesis is confirmed by our experiments (row two of Table 1).

In order to obtain an estimate of full system error, we can again use ray-tracing through the volume, and intersect the refracted rays

with a virtual Wavelet Noise background. The resulting images are then processed by the complete pipeline of optical flow, tomography, and Poisson integration. Row three in the table shows that the optical flow algorithm introduces additional error, but the overall error remains very low, especially when considering the lower bound provided by the Poisson solver. Figure 6 shows visualizations of the original ground truth flow, as well as the reconstructions with different numbers of cameras.

We also studied the impact of the anisotropic Poisson solver, and found that it improves the PSNR of tomographically reconstructed datasets by about 1 dB. For such datasets we found that a regularization value α of 0.8 produced the best results. All results in this paper were computed using this value.

Finally, we analyzed if it would be better to arrange the cameras in a full ring rather than the half ring we have used so far. The last row in Table 1 shows the results obtained with 7, 15, and 31 virtual cameras and approximated deflection vectors $\hat{\mathbf{d}}^{out}$. We chose an odd number of cameras for the full ring scenario in order to avoid almost complete redundancy of information when two cameras are opposite each other. The results in the table show almost no difference between the half and full ring setup for the same number of cameras. This justifies the use of the half ring setup, which is easier to realize physically.

Real measurements were performed in the setup described in Section 4. Figure 8 shows four time sequences of volume renderings for four different gas flows. The sequences demonstrate the ability of our system to capture both turbulent and laminar flows. The turbulent hot air flow above a burner in the top row clearly shows the advection of small scale detail over time. The laminar flows, including the hot air plumes above three tea lights in the bottom row, show the ability of our approach to clearly separate distinct features, as well as the temporal continuity and low noise present in our method. For the burner sequence, our most complex data set, we used approximately 150,000 basis functions and 700,000 pixel measurements per time frame. For the other sequences the linear system from Equation 5 is usually over-determined by a factor of 8 – 25.

In Figure 7 we show a collection of additional results. On the top left, we see a 2D deflection image obtained by measuring the disturbance that a jet of compressed air causes in the hot air plume created by a candle. Simulating such a flow would be difficult for most fluid simulators used in computer graphics, since this flow violates the incompressibility assumption. The top right of Figure 7 shows a potential use of captured flow data in computer graphics. In this image, the captured burner flow both distorts the rays of a synthetic camera, as well as the light rays originating from a synthetic light source. As a result, we see caustics projected onto a distorted wall. The bottom row of the figure shows the plumes of the three tea lights overlaid onto an original camera view, as well as a visualization of the 3D gradients for the turbulent burner flow.

We strongly encourage the reader to view the accompanying video, where we show additional results and animations for all shown sequences. Additionally, we show realistic renderings using the acquired dynamic data sets.

7 Conclusions

In this paper we have presented the first system for capturing non-stationary gas flows by observing the distortions they cause in camera images. In addition to this system, our contributions include a new way of synchronizing rolling shutter cameras for this purpose, as well as a novel algorithm for Schlieren tomography that works

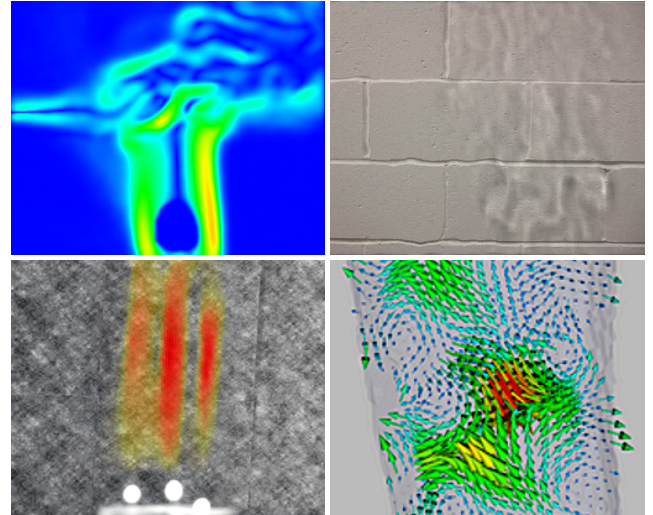


Figure 7: Additional results (see text).

with a modest number of views. Using these methods, it is now possible to capture complex non-stationary flows with very moderate hardware requirements.

We have demonstrated some initial uses of such captured flows in computer graphics. However, in the long run we believe that an even more interesting outcome of this line of work will be to provide ground truth information for validating fluid simulators and the heuristics they rely on. We also believe that it will be possible to fit fluid simulation parameters to the captured data, to steer fluid simulation to encompass certain characteristics of measured flow, and to develop data driven fluid simulation. These are interesting avenues of research that we would like to explore in the future.

8 Acknowledgments

We would like to thank the anonymous reviewers for their insightful comments.

Ivo Ihrke was supported by a Feodor-Lynen Fellowship of the Humboldt Foundation, Germany. Part of this work was supported by the National Sciences and Engineering Research Council of Canada (NSERC), and the German Research Council (DFG) under grant MA2555/5-1.

Appendix

Definition and Computation of the Diffusion Tensor The diffusion tensor is derived from the structure tensor [Weickert 1996] $\mathbf{J}_\sigma = K_\sigma * (\widehat{\nabla n} \widehat{\nabla n}^T)$ of the refractive index field with its components smoothed independently. We use a Gaussian filter kernel K_σ with $\sigma = 0.5$. Using an Eigen decomposition $\mathbf{J}_\sigma = \mathbf{V} \mathbf{A} \mathbf{V}^{-1}$, with $\lambda_0 \geq \lambda_1 \geq \lambda_2$, we generate the diffusion tensor by changing the eigenvalues to

$$\widetilde{\Lambda} = \begin{pmatrix} \alpha & & \\ & \alpha + (1 - \alpha)e^{-\frac{\max|\widehat{\nabla n}|}{k(\lambda_0 - \lambda_1)^2}} & \\ & & \alpha + (1 - \alpha)e^{-\frac{\max|\widehat{\nabla n}|}{k(\lambda_0 - \lambda_2)^2}} \end{pmatrix},$$

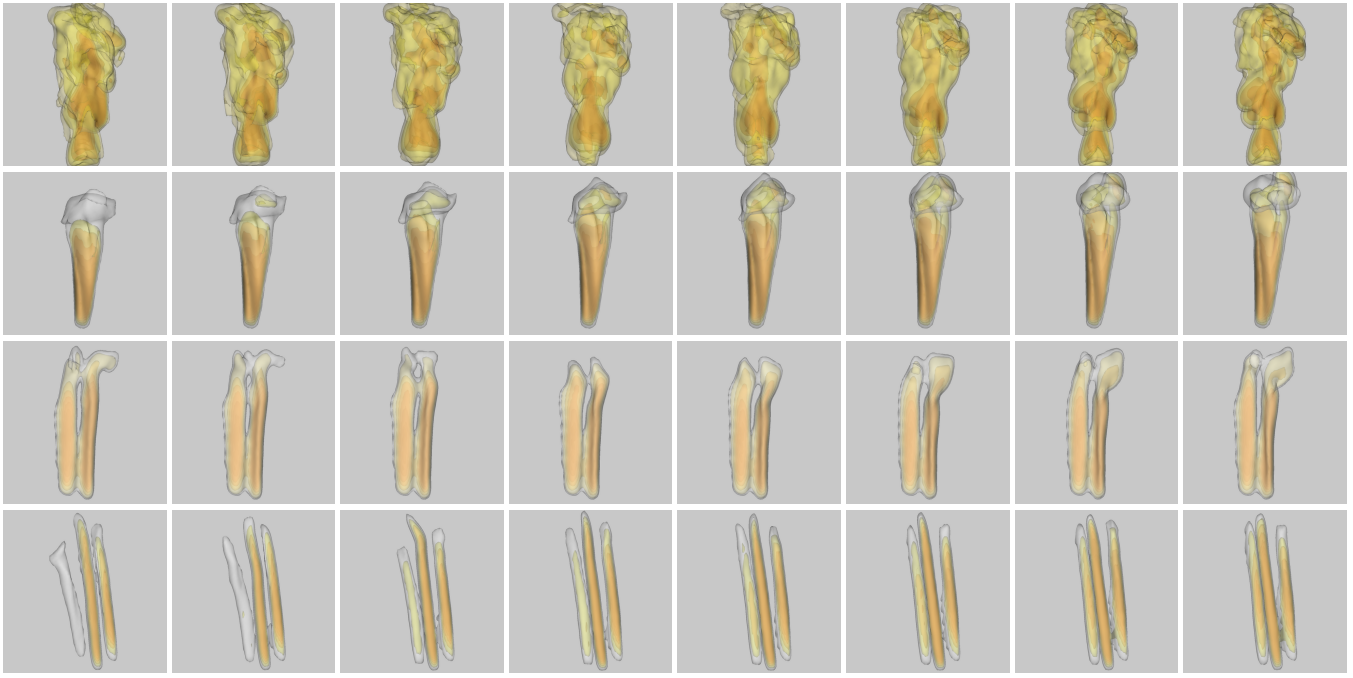


Figure 8: 3D reconstructions of data measured in our BOS tomography system. The images within each row are one frame (1/60 second) apart. Top row: a turbulent flow of hot air above a gas burner. The advection of features is clearly visible, as the hot air rises due to buoyancy. Second row: hot air rising from a candle. The flow starts out almost laminar, but eventually breaks up into more turbulent behavior. Third row: hot air plume for two tea lights. The almost laminar flow is occasionally disrupted by ambient air movement. Bottom row: very laminar flow above three tea lights. the individual hot air plumes are clearly visible.

where $k = 0.5 \cdot 10^{-5}$ and α is a data fidelity parameter. The diffusion tensor \mathbf{D} is obtained by computing $\mathbf{D} = \mathbf{V}\tilde{\Lambda}\mathbf{V}^{-1}$. Choosing $\alpha = 1$ results in standard Poisson integration which can be used if $\widehat{\nabla n}$ is indeed a gradient field; lower alpha values result in better noise removal. By analyzing tests on synthetic data we found $\alpha = 0.8$ to be a good choice for the noise levels introduced by optical flow and tomographic reconstruction, see Section 6.

References

- AGRAWAL, A., ALBERS, B., AND GRIFFIN, D. 1999. Abel inversion of Deflectometric Measurements in Dynamic Flows. *Applied Optics* 38, 15 (May), 3394–3398.
- AGRAWAL, A., RASKAR, R., AND CHELLAPPA, R. 2006. What Is the Range of Surface Reconstructions from a Gradient Field? In *Proc. ECCV*, 578–591.
- ATCHESON, B., HEIDRICH, W., AND IHRKE, I. 2008. An Evaluation of Optical Flow Algorithms for Background Oriented Schlieren Imaging. *Experiments in Fluids*. in print.
- BARRETT, R., BERRY, M., CHAN, T. F., DEMMEL, J., DONATO, J., DONGARRA, J., EIJKHOUT, V., POZO, R., ROMINE, C., AND DER VORST, H. V. 1994. *Templates for the Solution of Linear Systems: Building Blocks for Iterative Methods*, 2nd Edition. SIAM, Philadelphia, PA.
- BEN-EZRA, M., AND NAYAR, S. 2003. What Does Motion Reveal about Transparency? In *Proc. ICCV*, vol. 2, 1025–1032.
- BROX, T., BRUHN, A., PAPENBERG, N., AND WEICKERT, J. 2004. High Accuracy Optical Flow Estimation Based on a Theory for Warping. In *Proc. ECCV*, 25–36.
- CHUANG, Y., ZONGKER, D., HINDORFF, J., CURLESS, B., SALESIN, D., AND SZELISKI, R. 2000. Environment Matting Extensions: Towards Higher Accuracy and Real-Time Capture. In *Proc. SIGGRAPH*, 121–130.
- COOK, R., AND DEROSE, T. 2005. Wavelet Noise. *ACM Trans. Graphics (Proc. SIGGRAPH)* 24, 3 (July), 803–811.
- DALZIEL, S., HUGHES, G., AND SUTHERLAND, B. 2000. Whole-Field Density Measurements by 'Synthetic Schlieren'. *Experiments in Fluids* 28, 322–335.
- DE AGUIAR, E., STOLL, C., THEOBALT, C., AHMED, N., SEIDEL, H.-P., AND THRUN, S. 2008. Performance Capture from Sparse Multi-view Video. *ACM Trans. Graphics (Proc. SIGGRAPH)* 27, 3, article 98.
- DFG, SFB, 382. Fuel Injection volumetric data set. <http://www.volvis.org>.
- ELSINGA, G., OUDHEUSDEN, B., SCARANO, F., AND WATT, D. 2004. Assessment and Application of Quantitative Schlieren Methods: Calibrated Color Schlieren and Background Oriented Schlieren. *Experiments in Fluids* 36, 309–325.
- FARIS, G., AND BYER, R. 1988. Three-Dimensional Beam-Deflection Optical Tomography of a Supersonic Jet. *Applied Optics* 27, 24 (Dec.), 5202–5215.
- FUCHS, C., CHEN, T., GOESELE, M., THEISEL, H., AND SEIDEL, H.-P. 2006. Volumetric Density Capture From a Single Image. In *Proc. Volume Graphics*, 17–22.

- GOESELE, M., LENSCHE, H., LANG, J., FUCHS, C., AND SEIDEL, H.-P. 2004. DISCO: Acquisition of Translucent Objects. *ACM Trans. Graphics (Proc. SIGGRAPH)* 23, 3, 835–844.
- GOLDHAHN, E., AND SEUME, J. 2007. The Background Oriented Schlieren Technique: Sensitivity, Accuracy, Resolution and Application to a Three-Dimensional Density Field. *Experiments in Fluids* 43, 2–3, 241–249.
- GRANT, I. 1997. Particle Image Velocimetry: a Review. *Proceedings of the Institution of Mechanical Engineers* 211, 1, 55–76.
- GUTIERREZ, D., SERON, F. J., MUÑOZ, A., AND ANSON, O. 2006. Simulation of Atmospheric Phenomena. *Computers & Graphics* 30, 6, 994–1010.
- HASINOFF, S., AND KUTULAKOS, K. 2007. Photo-Consistent 3D Fire by Flame-Sheet Decomposition. *IEEE PAMI* 29, 5, 870–885.
- HAWKINS, T., EINARSSON, P., AND DEBEVEC, P. 2005. Acquisition of Time-Varying Participating Media. *ACM Trans. Graphics (Proc. SIGGRAPH)* 24, 3, 812–815.
- HORN, B., AND SCHUNCK, B. 1981. Determining Optical Flow. *Artificial Intelligence* 17, 185–203.
- HOWES, W. L. 1984. Rainbow Schlieren and its Applications. *Applied Optics* 23, 4, 2449–2460.
- IHRKE, I., AND MAGNOR, M. 2004. Image-Based Tomographic Reconstruction of Flames. *Proc. SCA*, 367–375.
- IHRKE, I., GOLDLUECKE, B., AND MAGNOR, M. 2005. Reconstructing the Geometry of Flowing Water. In *Proc. ICCV*, 1055–1060.
- IHRKE, I., ZIEGLER, G., TEVS, A., THEOBALT, C., MAGNOR, M., AND SEIDEL, H.-P. 2007. Eikonal Rendering: Efficient Light Transport in Refractive Objects. *ACM Trans. Graphics (Proc. SIGGRAPH)* 26, 3, article 59.
- JENSEN, H. W., MARSCHNER, S., LEVOY, M., AND HANRAHAN, P. 2001. A Practical Model for Subsurface Light Transport. In *Proc. SIGGRAPH*, 511–518.
- KAK, A. C., AND SLANEY, M. 2001. *Principles of Computerized Tomographic Imaging*. Society of Industrial and Applied Mathematics.
- KINDLER, K., GOLDHAHN, E., LEOPOLD, F., AND RAFFEL, M. 2007. Recent Developments in Background Oriented Schlieren Methods for Rotor Blade Tip Vortex Measurements. *Experiments in Fluids* 43, 2–3, 233–240.
- KUTULAKOS, K. N., AND STEGER, E. 2005. A Theory of Refractive and Specular 3D Shape by Light-Path Triangulation. In *Proc. ICCV*, 1448–1455.
- LAURENTINI, A. 1994. The Visual Hull Concept for Silhouette-Based Image Understanding. *IEEE PAMI* 16, 2 (Feb.), 150–162.
- LUCAS, B., AND KANADE, T. 1981. An Iterative Image Registration Technique with an Application to Stereo Vision. In *Proc. 7th Intl. Joint Conference on Artificial Intelligence*, 674–679.
- MARSCHNER, S., WESTIN, S., LAFORTUNE, E., TORRANCE, K., AND GREENBERG, D. 1999. Image-based BRDF Measurement Including Human Skin. In *Proc. EGWR*, 131–144.
- MATUSIK, W., PFISTER, H., BRAND, M., AND McMILLAN, L. 2003. A Data-Driven Reflectance Model. *ACM Trans. Graphics (Proc. Siggraph)* 22, 3, 759–769.
- MEIER, G. 2002. Computerized Background-Oriented Schlieren. *Experiments in Fluids* 33, 181–187.
- MIYAZAKI, D., AND IKEUCHI, K. 2005. Inverse Polarization Raytracing: Estimating Surface Shapes of Transparent Objects. In *Proc. CVPR*, vol. 2, 910–917.
- MORRIS, N. J. W., AND KUTULAKOS, K. N. 2005. Dynamic Refraction Stereo. In *Proc. ICCV*, 1573–1580.
- NARASIMHAN, S., GUPTA, M., DONNER, C., RAMAMOORTHI, R., NAYAR, S. K., AND JENSEN, H. W. 2006. Acquiring Scattering Properties of Participating Media by Dilution. *ACM Trans. Graphics (Proc. SIGGRAPH)* 25, 3, 1003–1012.
- RICHARD, H., AND RAFFEL, M. 2001. Principle and Applications of the Background Oriented Schlieren (BOS) Method. *Measurement Science and Technology* 12, 1576–1585.
- SCHARDIN, H. 1942. Die Schlierenverfahren und ihre Anwendungen. *Ergebnisse der Exakten Naturwissenschaften* 20, 303–439. English translation available as NASA TT F-12731, April 1970 (N70-25586).
- SCHOLZ, V., STICH, T., KECKEISEN, M., WACKER, M., AND MAGNOR, M. 2005. Garment Motion Capture Using Color-Coded Patterns. In *Proc. Eurographics*, 439–448.
- SCHWARZ, A. 1996. Multi-tomographic Flame Analysis with a Schlieren Apparatus. *Measurement Science and Technology* 7, 406–413.
- SETTLES, G. S. 2001. *Schlieren and Shadowgraph Techniques*. Experimental Fluid Mechanics. Springer.
- STAM, J., AND LANGUÉNOU, E. 1996. Ray-tracing in Non-Constant Media. In *Proc. EGSR*, 225–234.
- TRIFONOV, B., BRADLEY, D., AND HEIDRICH, W. 2006. Tomographic Reconstruction of Transparent Objects. In *Proc. EGSR*, 51–60.
- VAN VLIET, E., VAN BERGEN, S., DERKSEN, J., PORTELA, L., AND VAN DEN AKKER, H. 2004. Time-Resolved, 3D, Laser-Induced Fluorescence Measurements of Fine-Structure Passive Scalar Mixing in a Tubular Reactor. *Experiments in Fluids* 37, 1–21.
- VENKATAKRISHNAN, L., AND MEIER, E. 2004. Density Measurements using the Background Oriented Schlieren Technique. *Experiments in Fluids* 37, 237–247.
- VLASIC, D., BARAN, I., MATUSIK, W., AND POPOVIĆ, J. 2008. Articulated Mesh Animation from Multi-view Silhouettes. *ACM Trans. Graphics (Proc. SIGGRAPH)* 27, 3, article 97.
- WARD, G. 1992. Measuring and Modeling Anisotropic Reflection. In *Proc. SIGGRAPH*, 265–272.
- WEICKERT, J. 1996. *Anisotropic Diffusion in Image Processing*. PhD thesis, Dept. of Mathematics, University of Kaiserslautern.
- WHITE, R., CRANE, K., AND FORSYTH, D. 2007. Capturing and Animating Occluded Cloth. *ACM Trans. Graphics (Proc. SIGGRAPH)* 26, 3, article 34.
- WILBURN, B., JOSHI, N., VAISH, V., LEVOY, M., AND HOROWITZ, M. 2004. High-Speed Videography Using a Dense Camera Array. In *Proc. CVPR*, II-294–II-301.
- ZHANG, Z. 1999. Flexible Camera Calibration By Viewing a Plane From Unknown Orientations. In *Proc. ICCV*, 666–673.